Green Chemistry

PAPER

View Article Online
View Journal | View Issue

Cite this: *Green Chem.*, 2025, **27**, 12785

An activity–selectivity–stability-balanced bifunctional high-entropy phosphide for overall seawater splitting at industrial-level current density

Changrui Feng,*†[a] Yifan Zhou,†[b] Shuying Li,[b] Yuxia Jin,[b] Meng Chen,[c] Rui Yang,[b] Wenjia Zhou,[b] Zhengkun Xie,*[d] Xiumin Li,[e] Xiangyu Chen,[f] Wenhao Lian,[g] Abuliti Abudula[b] and Guoqing Guan *[b]

Seawater electrolysis is considered as a promising pathway to substitute freshwater electrolysis for large-scale sustainable and clean hydrogen production. However, conventional electrocatalyst materials often suffer from severe corrosion and performance degradation in high-salinity environments mainly due to the presence of aggressive chloride ions. Besides, the chloride ion-induced competitive anodic chlorine evolution reaction also needs to be avoided since it can lead to low electrolysis efficiency. The application of high-entropy materials (HEMs) offers a potential solution to these challenges. The unique compositional complexity endows HEMs with remarkable properties including significantly enhanced resistance to corrosion and improved catalytic activity, allowing them to exhibit excellent stability and efficiency in the seawater electrolysis process. Herein, a metal–organic framework-derived high-entropy NiCoFeMnCu phosphide/carbon ($(NiCoFeMnCu)_2P/C$) composite with a three-dimensional structure was *in situ* prepared on a nickel foam (NF) substrate for achieving highly active and stable seawater splitting. As a result, the ultralow overpotentials of 88/195 mV (hydrogen evolution reaction (HER)/oxygen evolution reaction (OER)) in alkaline freshwater and 100/223 mV (HER/OER) in alkaline seawater at 10 mA cm^{-2} were obtained, revealing its exceptional bifunctional performances. Furthermore, a two-electrode electrolyzer assembled by using $(NiCoFeMnCu)_2P/C/NF$ demonstrated continuous stable operation for 480 h at an industrial-level current density (1 A cm^{-2}) without obvious activity decay, and almost no hypochlorite species were detected in the alkaline seawater electrolyte, confirming its robust chloride resistance and high selectivity. Therefore, this $(NiCoFeMnCu)_2P/C$ electrocatalyst should be a promising bifunctional electrocatalyst for overall seawater splitting.

Received 20th July 2025,
Accepted 9th September 2025

DOI: 10.1039/d5gc03723a

rsc.li/greenchem

Green foundation

1. This work directly leverages abundant seawater as sustainable feedstock for sustainable green hydrogen production, avoiding freshwater consumption and geographical limitations.
2. The MOF-derived high-entropy $(NiCoFeMnCu)_2P/C$ catalyst uniquely integrates multi-metal synergy for intrinsic activity, a protective conductive carbon matrix inhibiting chloride penetration and enhancing charge transfer as well as *in situ* reconstructed MOOH layers acting as active sites and providing a corrosion-resistant shield. This synergy critically reconciles activity–selectivity–stability trade-offs, minimizing undesirable hypochlorite production and catalyst degradation.
3. Future research will be dedicated to (i) further improving cathodic HER performance, (ii) deeper exploration of the reaction mechanism, and (iii) employing neutral seawater as the electrolyte to investigate its electrolysis performance for reducing the need for additional strong alkali, thus making the process more environmentally friendly and economically viable.

[a]*Hubei Key Laboratory of Pollutant Analysis & Reuse Technology, College of Chemistry and Chemical Engineering, Hubei Normal University, No. 11, Cihu Road, Huangshi, Hubei 435002, China. E-mail: fengcr@hbnu.edu.cn*
[b]*Graduate School of Science and Technology/Institute of Regional Innovation, Hirosaki University, 3-Bunkyocho, Hirosaki 036-8561, Japan. E-mail: guan@hirosaki-u.ac.jp*
[c]*College of Chemistry and Chemical Engineering, Xi'an University of Science and Technology, No. 58, Yanta Middle Road, Beilin District, Xi'an 710054, China*
[d]*College of Chemistry, Zhengzhou University, Kexue Avenue 100, Zhengzhou, Henan 450001, China. E-mail: xie@zzu.edu.cn*
[e]*School of Materials Science and Engineering, Zhengzhou University, Kexue Avenue 100, Zhengzhou, Henan 450001, China*
[f]*Longdu Laboratory for New Chemical Materials, Puyang, Henan Province, 457000, China*
[g]*Shanxi Research Institute for Clean Energy, Tsinghua University, Taiyuan, 030032, China*
† These two authors contributed equally to this work.

Introduction

Water electrolysis powered by renewable electricity stands as the most attractive and extensively studied zero-carbon hydrogen production pathway.[1–4] However, conventional freshwater electrolysis suffers from severe scalability constraints due to dwindling freshwater resources.[5,6] In comparison, the ocean covers approximately 71% of the Earth's surface and is the largest source of hydrogen on the planet.[7] Leveraging Earth's rich seawater reserves to achieve direct seawater splitting for hydrogen generation offers an abundant and sustainable alternative.[8,9] Nevertheless, the complex composition of natural seawater, which contains not only corrosive chloride ions (Cl^-, ≈0.5 M) but also dissolved impurities (*e.g.*, Ca^{2+} and Mg^{2+}), imposes multifaceted challenges for electrocatalyst design under practical operational conditions.[10] These components trigger three primary degradation pathways: (i) chloride-induced corrosion leading to metal dissolution that accelerates catalytic activity degradation; (ii) undesired reaction dominance, particularly the chloride evolution reaction (CER, $Cl^- + 2OH^- \rightarrow ClO^- + H_2O + 2e^-$), which kinetically competes with the oxygen evolution reaction (OER) due to a potential difference of only about 480 mV, reducing faradaic efficiency (FE); and (iii) catalyst deactivation through the formation of insoluble precipitates ($Mg(OH)_2$ and $Ca(OH)_2$), which block active sites and increase ohmic resistance.[11,12] Correspondingly, realizing practical seawater electrolysis demands electrocatalysts engineered with triple functionality including corrosion resistance, abundant reactive sites and selective ion oxidation.

Recent research highlights high-entropy materials (HEMs) as a paradigm-shifting design strategy for electrocatalysts in the field of energy storage and conversion.[13,14] The high-entropy configuration endows catalysts with two critical properties crucial for seawater electrolysis. The first is enhanced structural stability *via* the sluggish diffusion effect. Specifically, the multi-principal-element composition induces a complex and varied atomic environment, significantly increasing energy barriers for elemental diffusion and degradation. This effect stabilizes the catalyst against dissolution, agglomeration, and chloride corrosion, which is conducive to long-term operation in seawater electrolyte.[15,16] Second, the multi-principal-element composition can achieve synergistic modulation of the electronic structure to accelerate reaction kinetics. The complex chemical environment created by the mixing of multiple elements allows fine-tuning of the electronic structure of active sites, potentially optimizing the adsorption/desorption behavior of reaction intermediates.[17,18] Such properties ideally align with the operational demands of seawater electrolysis catalysts. Despite these merits, synthesizing HEMs with precise compositional control and high surface area remains challenging.

Metal–organic frameworks (MOFs) usually exhibit high specific surface areas, tunable porosity, and abundant active sites that offer ideal sacrificial templates to engineer high-entropy derivatives while preserving structural advantages.[19] Furthermore, pyrolysis of MOFs often generates a carbon layer on their surfaces,[20] which not only enhances conductivity but also acts as a protective layer against chloride corrosion in aggressive seawater electrolyte. In particular, it is reported that MOF-derived transition metal phosphides (TMPs) could serve as promising bifunctional electrocatalysts while synergistically integrating enhanced electrical conductivity with accelerated charge transfer.[21,22] Moreover, the P atom with a negative charge always serves as a proton acceptor and plays a significant role in weakening the metal–hydride bond strength.[23,24] Therefore, in contrast to pure metals with considerably strong adsorption, the moderate bonding between P and the reaction intermediates is more conducive to hydrogen desorption.[25] Indeed, using MOFs as precursors also enables the synthesis of compounds such as transition metal oxides (TMOs), sulfides (TMSs), and nitrides (TMNs), which often possess their own respective catalytic advantages.[26,27] The persistent preference for TMPs can be primarily explained as follows. First, TMPs often exhibit metal-like physicochemical properties with high electrical conductivity, thus demonstrating excellent catalytic activity.[28] Although TMOs generally possess very good stability, they often suffer from poor electrical conductivity and low intrinsic activity.[29] Second, introducing P element can significantly improve the stability of transition metal-based electrocatalysts and reduce metal dissolution thermodynamically, which is due to the strong covalent M–P bonding that prevents sample degradation.[30,31] Meanwhile, TMSs and TMNs are often hampered by poor stability although they frequently demonstrate considerable catalytic activity.[32,33] In addition, Bodhankar *et al.*[34] summarized that, although TMPs do not exhibit top-tier performance in any single catalytic metric, they demonstrate a balanced and competitive performance across all key indicators with no significant weaknesses, making them the most versatile and ideal candidate materials.

For the design of high-entropy catalysts, element selection is a crucial step. Compared with other transition metal elements, Ni and Co possess many advantages such as good conductivity, abundant active sites, high active surface area and low cost that make them ideal electrocatalysts for water splitting, typically exhibiting excellent electrocatalytic activity.[35,36] Therefore, these two elements can be initially selected as the foundational components for constructing high-entropy materials. Fe is a well-known electronic structure modulator for Ni/Co-based catalysts. Its incorporation can optimize the adsorption energy of oxygen intermediates (*e.g.*, *O and *OH), thereby enhancing OER kinetics.[37] Mn is a transition metal element that can exist in multiple stable valence states, such as +4, +3, and even +2, in compounds; therefore, it can effectively modulate the electronic structure.[38,39] Additionally, it has been reported that Mn can enhance the catalyst's selectivity toward OH^- and improve the catalyst's corrosion resistance in seawater electrolyte.[40] Cu is always selected mainly for its good electrical conductivity to further accelerate OER and HER kinetics during seawater electrolysis.[41]

Herein, we bridge these frontiers by developing a MOF-derived high-entropy phosphide (HEP) as a bifunctional electrocatalyst for efficient and stable overall seawater splitting.

This electrocatalyst integrates five transition metals (Ni, Co, Fe, Mn, and Cu) within a single-phase phosphide architecture, leveraging compositional synergy to optimize catalytic activity for both the HER and the OER. By first synthesizing a multi-metallic MOF precursor through a hydrothermal method followed by a controlled phosphating process, a high-entropy phosphide/carbon structure ($(NiCoFeMnCu)_2P/C$) with high-density active sites and chloride-resistant surfaces is achieved. Crucially, the high-entropy effect promotes the stabilization of the phosphide lattice against phase segregation during the operation. When applied to seawater electrolysis, it achieves a functional trade-off among catalytic activity, reaction selectivity, and operational stability. Electrochemical evaluations confirm its exceptional bifunctionality with ultralow overpotentials of 88/100 mV (HER) and 195/223 mV (OER) at 10 mA cm^{-2} in alkaline water/seawater electrolysis. It also sustains 480 hours of continuous operation with negligible decay in alkaline seawater electrolyte at an industrial-level current density of 1 A cm^{-2}. Besides, characterization of the spent catalyst confirms the reconstruction of a HEP with the formation of metal oxyhydroxides on the electrocatalyst surface, which serve as active sites while resisting chloride corrosion. This strategy establishes a versatile platform for designing high-entropy-stabilized electrocatalysts toward sustainable hydrogen production from complex feedstocks.

Experimental section

Chemicals

Nickel(II) chloride hexahydrate ($NiCl_2{\cdot}6H_2O$, ≥98.0%), cobalt(II) chloride hexahydrate ($CoCl_2{\cdot}6H_2O$, ≥99.0%), manganese(II) chloride tetrahydrate ($MnCl_2{\cdot}4H_2O$, ≥99.0%), iron(II) chloride tetrahydrate ($FeCl_2{\cdot}4H_2O$, ≥99.0%), copper(II) chloride dihydrate ($CuCl_2{\cdot}2H_2O$, ≥99.0%), hydrochloric acid (HCl, 35–37%), *N*,*N*-diethyl-1,4-phenylenediamine (DPD, ≥95.0%), potassium hydroxide (KOH, ≥85.0%), *N*,*N*-dimethylformamide (DMF, ≥99.5%) and ethanol (C_2H_5OH, ≥99.5%) were purchased from Wako, Japan. Sodium hypophosphite (NaH_2PO_2, ≥99%) was obtained from Sigma-Aldrich. Terephthalic acid (>99.0%) was ordered from TCI, Japan. The nickel foam (NF) used in this work was provided by MTI, Japan, and the detailed technical parameters including thickness, PPI (pores per inch), and bulk density are 1.5 mm, 110 and 0.23 g cm^{-3}, respectively. The seawater was fetched from the Sea of Japan, Aomori (Fig. S1).

Synthesis of the $(NiCoFeMnCu)_2P/C$ electrocatalyst on NF

First, the MOF precursor was synthesized *in situ* on a NF substrate *via* a one-step solvothermal process. Generally, 0.5 mmol of $NiCl_2{\cdot}6H_2O$, 0.5 mmol of $CoCl_2{\cdot}6H_2O$, 0.5 mmol of $FeCl_2{\cdot}4H_2O$, 0.5 mmol of $MnCl_2{\cdot}4H_2O$, 0.5 mmol of $CuCl_2{\cdot}2H_2O$ and 3 mmol of organic ligand (terephthalic acid) are dissolved in a mixed solvent of DMF (25 mL), distilled water (2 mL) and ethanol (2 mL). The obtained mixed homogeneous solution after stirring for 30 min was transferred into an autoclave and placed into an oven for heating at 120 °C for 12 h. After cooling to room temperature and washing with ethanol 3 times, a multi-metallic MOF coating on NF was obtained. Thereafter, 1 g of NaH_2PO_2 and the dried MOF precursor/NF were placed individually in two porcelain boats, which were fed into a tube furnace at the upstream and downstream sides, respectively. Phosphating was conducted at 350 °C for 2 h under an Ar atmosphere at a heating rate of 5 °C min^{-1}. Finally, the furnace was cooled to room temperature to obtain the $(NiCoFeMnCu)_2P/C/NF$ electrode.

Control sample preparation

To verify the high catalytic activity of the HEP, control samples including $Ni_2P/C/NF$, $(NiCo)_2P/C/NF$, $(NiCoFe)_2P/C/NF$, and $(NiCoFeMn)_2P/C/NF$ electrodes were also prepared. The preparation processes were the same as that of $(NiCoFeMnCu)_2P/C/NF$, except without the addition of the corresponding metal chlorides for the absent metals.

Electrocatalyst characterization

The whole morphology of the as-synthesized electrocatalysts was observed through a scanning electron microscope (SEM, JEOL JSM-7000F, AV: 10 kV). The nanostructure and elemental mapping were recorded using a transmission electron microscope (TEM, JEOL JEM-2100, AV: 200 kV) equipped with an energy-dispersive X-ray spectrometer (EDS). Inductively coupled plasma optical emission spectrometry (ICP-OES) was employed to quantify the exact atomic ratio of those metal elements in the electrocatalyst. To verify whether it is a single phase, the crystal structure of the electrocatalyst was determined using an X-ray powder diffraction instrument (XRD, Rigaku SmartLab diffractometer) with Cu-Kα as the radiation source (scanning range of 2θ: 10°–90°). X-ray photoelectron spectroscopy (XPS) was conducted to reveal the valence states of the main elements of the as-prepared sample using a VG Scientific ESCALab250i-XL instrument (excitation source: monochromated Al Kα). Raman spectroscopy was performed to further confirm the chemical structure using a Jasco NRS-5500 laser Raman spectrophotometer with an excitation wavelength of 532 nm.

Electrochemical performance evaluation

All electrochemical tests were conducted on a Squidstat Plus potentiostat equipped with a three-electrode system, in which the as-prepared electrode was used as the working electrode while a standard Hg/HgO electrode (E° = 0.098 V) and a carbon rod acted as the reference and counter electrodes, respectively. Before linear sweep voltammetry (LSV), the electrode was first activated through cyclic voltammetry (CV) in the range of 0–1.5 V *vs.* Hg/HgO for 20 cycles to obtain a stable curve. After that, the OER polarization curve was obtained from LSV under reverse scan in the potential range of 1.5–0 V *vs.* Hg/HgO. Similarly, CV activation for the HER test was performed in the range of −0.5 to −1.5 V, and the potential of LSV was also scanned from −0.5 to −1.5 V. Electrochemical impedance spectroscopy (EIS), which can be employed to reveal the interfacial

charge transfer, was performed in the frequency range of 10 mHz–10 kHz at a constant potential of 0.6 V. CV tests at different scan rates of 20, 40, 60, 80 and 100 mV s^{-1} were carried out in the non-faradaic range of 0.05–0.15 V to determine the double-layer capacitance (C_{dl}). Then, the obtained C_{dl} values were incorporated into the following equation to calculate the electrochemical surface area (ECSA):

$$\mathrm{ECSA} = C_{dl}/C_s$$

where C_s is the specific capacitance of a flat surface (40 μF cm^{-2}).[42] In this work, all measured potentials were converted to the reversible hydrogen electrode (RHE) scale using the equation E(*vs.* RHE) = E(*vs.* Hg/HgO) + 0.059 pH + 0.098 with 70% *iR* compensation (a higher percentage of compensation will cause excessive noise in the test curve) through the manual correction method and the final potential was calculated as E(*vs.* RHE) = E(*vs.* Hg/HgO) + 0.059 pH + 0.059–70% iR_s.

Results and discussion

Morphological and structural characterization

The electrode fabrication process is schematically illustrated in Fig. 1, which is composed of two steps. First, five kinds of metal chlorides and terephthalic acid are self-assembled to form a multi-metallic MOF precursor on NF through a solvothermal method. Then, the obtained MOF precursor/NF electrode and NaH_2PO_2 powders are separately placed downstream and upstream in a tube furnace for phosphating. As the temperature gradually increases, NaH_2PO_2 decomposes to produce PH_3 for phosphating the precursor while the organic ligands convert into carbon in the high-entropy phosphide matrix. As such, the $(NiCoFeMnCu)_2P$/C/NF electrode is obtained.

The SEM images (Fig. 2a and b) show that the as-synthesized $(NiCoFeMnCu)_2P$/C, featuring an irregular nanosheet morphology, is uniformly grown and fully covers NF, which is similar to the as-synthesized monometallic to tetrametallic phosphides (Fig. S2–S5). To estimate whether it is a high-entropy material, the critical factor, *i.e.*, the crystal structure, was determined. The XRD pattern of the MOF precursor was first recorded and shows good consistency with MIL-101 (Fig. S6).[43] As shown in Fig. 2c, the diffraction peaks of the as-synthesized high-entropy catalyst appeared in the range of 40° to 90° and are in good agreement with those of Ni_2P (JCPDS#03-0953). In addition, there is a wide peak located around 20° that should be attributed to amorphous carbon,[44] which manifests that carbon was generated in the high-entropy catalyst during the pyrolysis process due to the existence of organic ligands. The XRD patterns of the other control samples as depicted in Fig. S7 and Table S1 were also found to exhibit a single phase of Ni_2P. The atomic ratios of all metallic elements in HEP/C are further confirmed by ICP-OES analysis to be in the defined range of 5%–35%, which is also a critical factor for any HEMs (Fig. S8). Then, the recorded Raman spectra as shown in Fig. 2d were analyzed to investigate the structures of the MOF precursor and HEP/C. As for the MOF precursor, three vibrational peaks are observed at *ca.* 861, 814, and 633 cm^{-1}, which are attributed to the C–H stretching region of the benzene ring of the ligands.[45] Besides, two peaks appeared at *ca.* 1612 and 1421 cm^{-1} corresponding to the in- and out-of-phase stretching regions of the carboxylate groups, respectively.[46] However, these characteristic peaks derived from the organic ligands (*i.e.*, terephthalic acid) all disappear

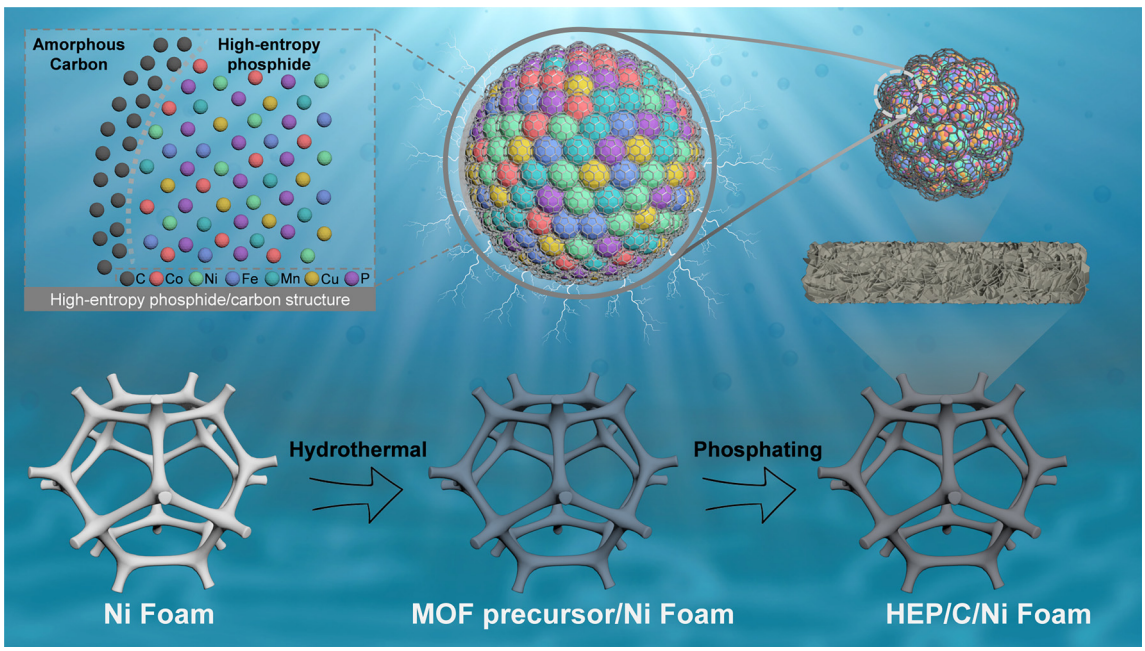

Fig. 1 Schematic illustration of $(NiCoFeMnCu)_2P$/C/NF electrode preparation.

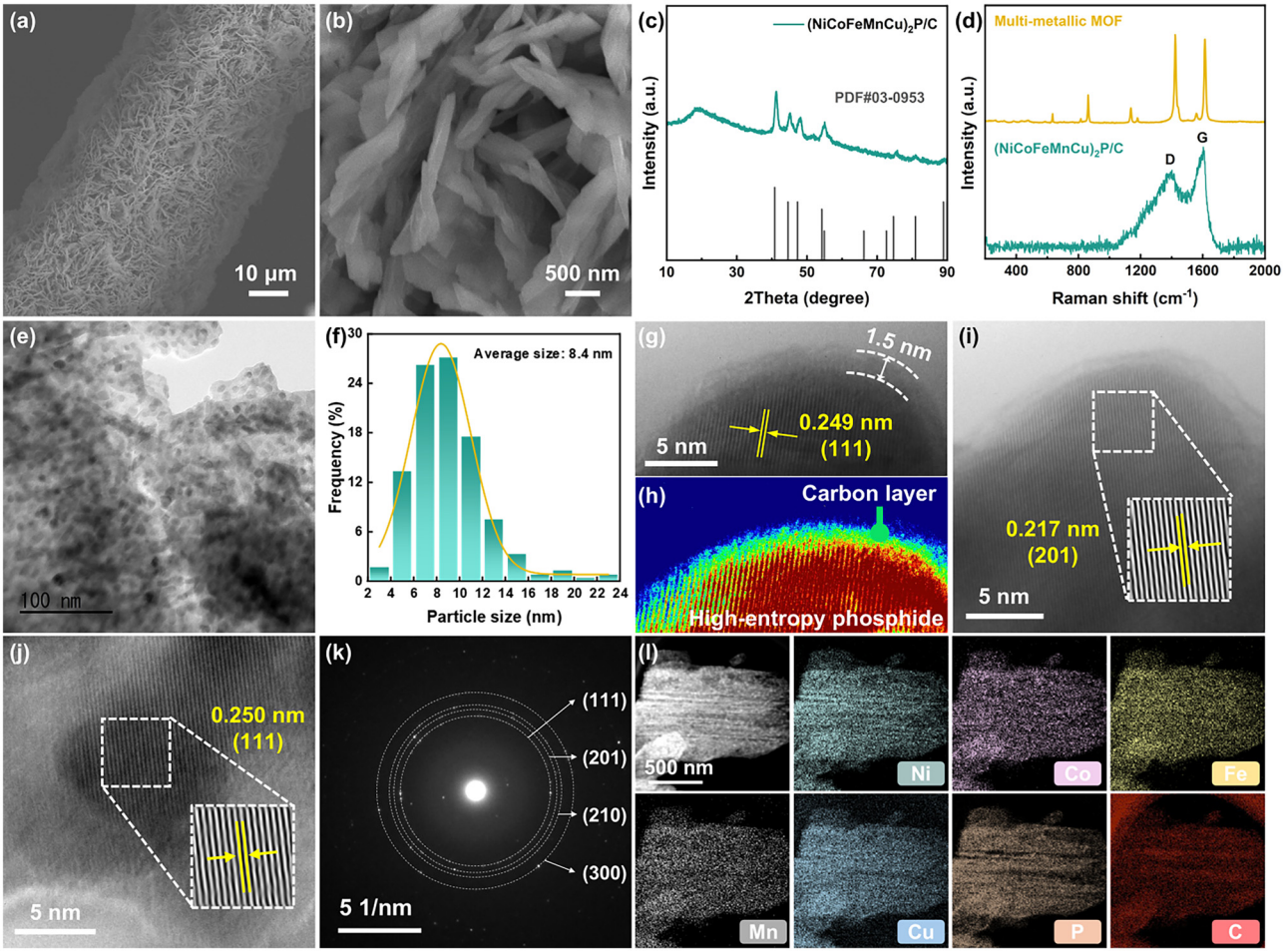

Fig. 2 Morphological and structural characterization of the as-synthesized high-entropy catalyst. (a and b) SEM images; (c) XRD patterns; (d) Raman spectrum; (e) TEM image; (f) particle size distribution histogram; (g) HRTEM image and (h) simulated thermal view; (i and j) HRTEM images; (k) FFT pattern and (l) EDX mappings of HEP/C nanosheets.

after phosphating, and instead two prominent peaks of D and G bands located at ~1370 and ~1600 cm^{-1} are observed (Fig. 2d). These characteristics should be derived from graphitic (or, at least, sp^2-based) carbons, which further indicate the conversion of organic ligands into carbon.[47] The above results preliminarily demonstrate that the as-synthesized electrocatalyst should be a HEP/C composite.

The TEM image in Fig. 2e clearly shows the nanostructure of HEP/C. It can be seen that the nanosheets are composed of small nanoparticles with a diameter of about 8.4 nm (Fig. 2f), coated with a carbon layer. Moreover, there are irregular spaces among these nanoparticles, which are conducive to electrolyte transport and gas release. By enlarging the nanoparticles at the edges, an amorphous carbon layer with a thickness of ~1.5 nm can be observed, and the clear lattice fringe inside shows a spacing of 0.249 nm, which corresponds to the (111) plane of Ni_2P (Fig. 2g). The simulated thermal view (Fig. 2h) further makes the distinction between the amorphous and crystalline areas clearer, which confirms that the nanostructure consists of an amorphous carbon layer surrounding the crystalline high-entropy phosphide nanoparticle. Other regions are also examined to further observe the lattice fringes, with measured interplanar spacings of 0.217 and 0.250 nm, matching well with the (201) and (111) crystal planes, respectively (Fig. 2i and j). Meanwhile, the selected-area electron diffraction (SAED) pattern demonstrates a series of diffraction rings matching well with the (111), (201), (210) and (300) planes of Ni_2P (Fig. 2k). The energy dispersive X-ray spectroscopy (EDX) elemental mapping (Fig. 2l) demonstrates the uniform distribution of all elements in the as-prepared electrocatalyst. By integrating all the above characterization results, it can be verified that the HEP/C composite structure has been successfully synthesized.

Surface chemical valence states

The surface elemental compositions and their valence states of the as-synthesized MOF precursor and HEP/C were investigated by XPS analysis (Fig. S9 and Fig. 3). From the wide-scan XPS spectrum (Fig. 3a), the corresponding characteristic peaks belonging to Ni 2p, Fe 2p, Co 2p, Mn 2p, Cu 2p, P 2p and C 1s

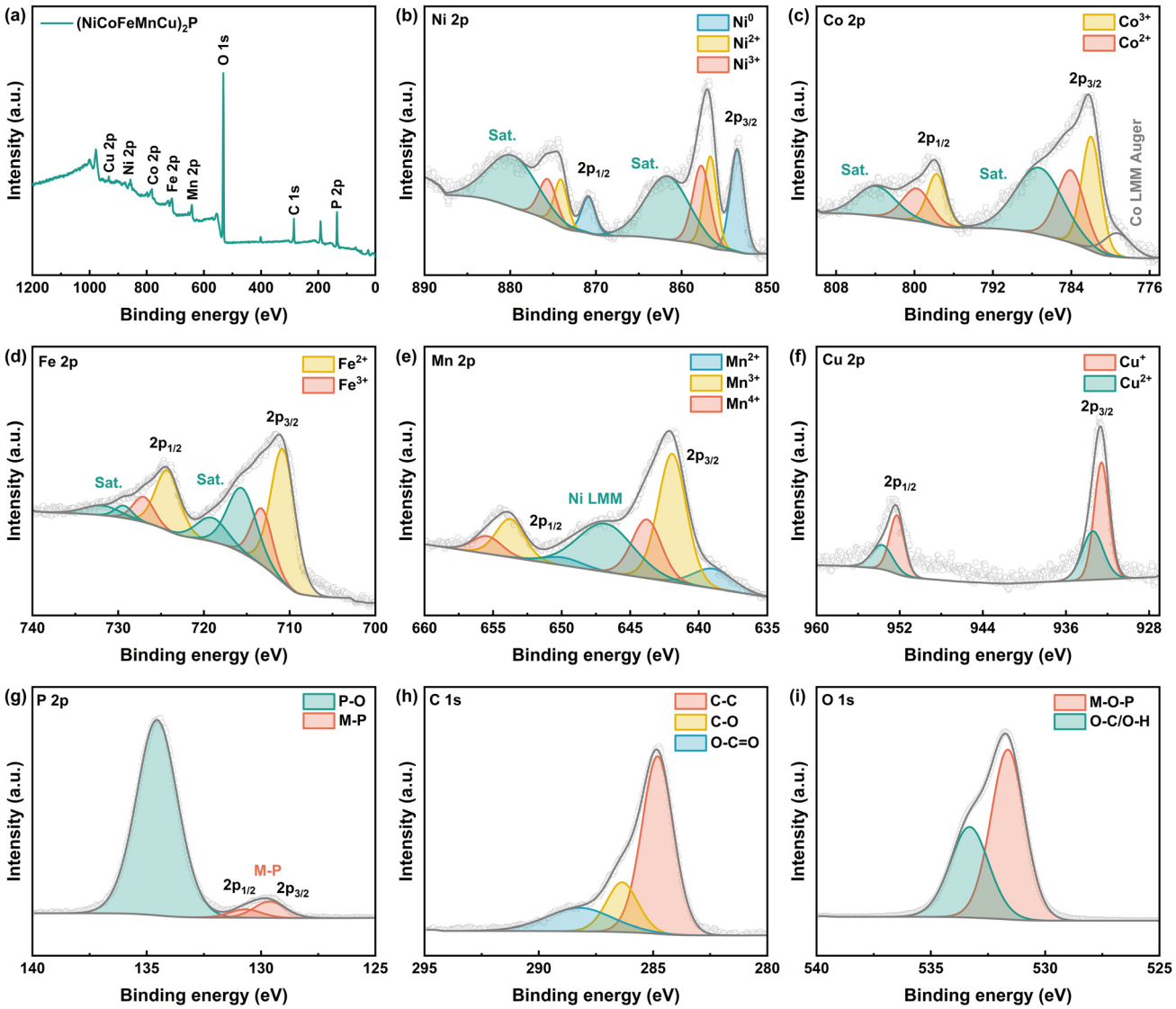

Fig. 3 XPS analysis of $(NiCoFeMnCu)_2P$. (a) Wide-scan XPS spectra and high-resolution XPS spectra for (b) Ni 2p, (c) Co 2p, (d) Fe 2p, (e) Mn 2p, (f) Cu 2p, (g) P 2p, (h) C 1s and (i) O 1s.

are all detected, which are consistent with the elemental mapping analysis results. A discernible O 1s peak in the XPS spectrum is attributed to inevitable surface oxidation of the phosphide catalyst upon air exposure.[48,49] The high-resolution XPS spectra of these elements were further obtained to investigate their surface chemical valence states. As demonstrated in Fig. 3b, the high-resolution XPS spectrum of Ni 2p is roughly separated into $2p_{1/2}$ and $2p_{3/2}$ spin–orbit doublets and two shake-up satellites, whereas the two spin–orbit doublets are deconvoluted into three pairs of peaks, which correspond to three valence states of Ni. Specifically, the first pair located at 853.53/870.88 eV should be assigned to Ni^0, and the adjacent second pair and the third pair are associated with Ni^{2+} (856.65/874.09 eV) and Ni^{3+} (857.70/875.63 eV), respectively.[50] The fitted high-resolution Co 2p XPS spectrum displayed in Fig. 3c includes two pairs of doublets situated at 781.99/797.73 eV and 784.05/799.79 eV, which are attributed to Co^{3+} and Co^{2+}, respectively, also with a Co LMM Auger peak at 779.33 eV.[51] It is worth noting that Co^{3+} sites are known to play a crucial role in promoting the formation of HOO* intermediates during the OER process, thereby enhancing the reaction rate.[52] Two remaining peaks situated at 789.50 and 880.52 eV are referred to as satellites. As for the Fe 2p spectrum (Fig. 3d), the pair of peaks at lower binding energies (*ca.* 710.78/724.24 eV) corresponds to Fe^{2+}, while the pair at 713.25/727.02 eV is related to Fe^{3+} with four satellites observed at 715.56, 729.36, 719.06 and 731.86 eV.[53,54] The high-resolution XPS spectrum of Mn 2p after peak differentiation in Fig. 3e indicates the coexistence of three valence states of Mn species on the HEP/C catalyst surface, with binding energies of 638.96/649.91, 641.94/653.74 and 643.79/655.43 eV, respectively, correlating with Mn^{2+}, Mn^{3+} and Mn^{4+}. Here, the appearance of high-valent Mn^{4+} was

reported to help improve electrical conductivity and energy conversion efficiency.[55] Fig. 3f displays the high-resolution XPS spectrum of Cu 2p composed of two spin–orbit doublets, in which the deconvoluted peaks located at 932.59/952.27 and 933.42/953.69 eV are the characteristic peaks of Cu^{+} and Cu^{2+}, respectively.[56] The XPS spectrum of P (Fig. 3g) shows two peaks at 129.62 and 130.67 eV, which are related to P $2p_{1/2}$ and $2p_{3/2}$ associated with the metal–P bond (M–P) formation. Besides, the appearance of P–O at 134.55 eV indicates that the catalyst should be partially oxidized upon exposure to air.[57] Here, it can be seen that all metallic elements exhibit varying oxidation states, suggesting that electron transfer has taken place between them and P atoms. As shown in Fig. 3h, the XPS spectrum of C 1s exhibits three peaks at 284.80, 286.35 and 288.22 eV, corresponding to C–C, C–O and O–C=O, respectively,[58] which is because those benzene species and carboxyl groups from the organic ligand are converted to carbon species during the phosphating process. The O 1s spectrum (Fig. 3i) is also fitted, and the peak located at 531.64 eV is assigned to M–O–P, further confirming partial surface oxidation and is consistent with the XPS spectrum of P 2p.[21]

Catalytic performance in alkaline water/seawater electrolysis

After characterization of the morphology and structure of the as-prepared high-entropy phosphide electrocatalyst, an electrochemical test was further performed to evaluate its catalytic performance in 1 M KOH freshwater-based electrolyte. As demonstrated in Fig. 4a, it can be clearly observed that the high-entropy $(NiCoFeMnCu)_2P/C/NF$ electrode exhibits significantly boosted OER performance compared with the control samples from the LSV curves. The overpotential required to achieve a current density of 10 mA cm^{-2} is only 195 mV, which is considerably lower than those of $Ni_2P/C/NF$ (264 mV), $(NiCo)_2P/C/NF$ (287 mV), $(NiCoFe)_2P/C/NF$ (247 mV) and $(NiCoFeMn)_2P/C/NF$ (202 mV), as summarized in the histo-

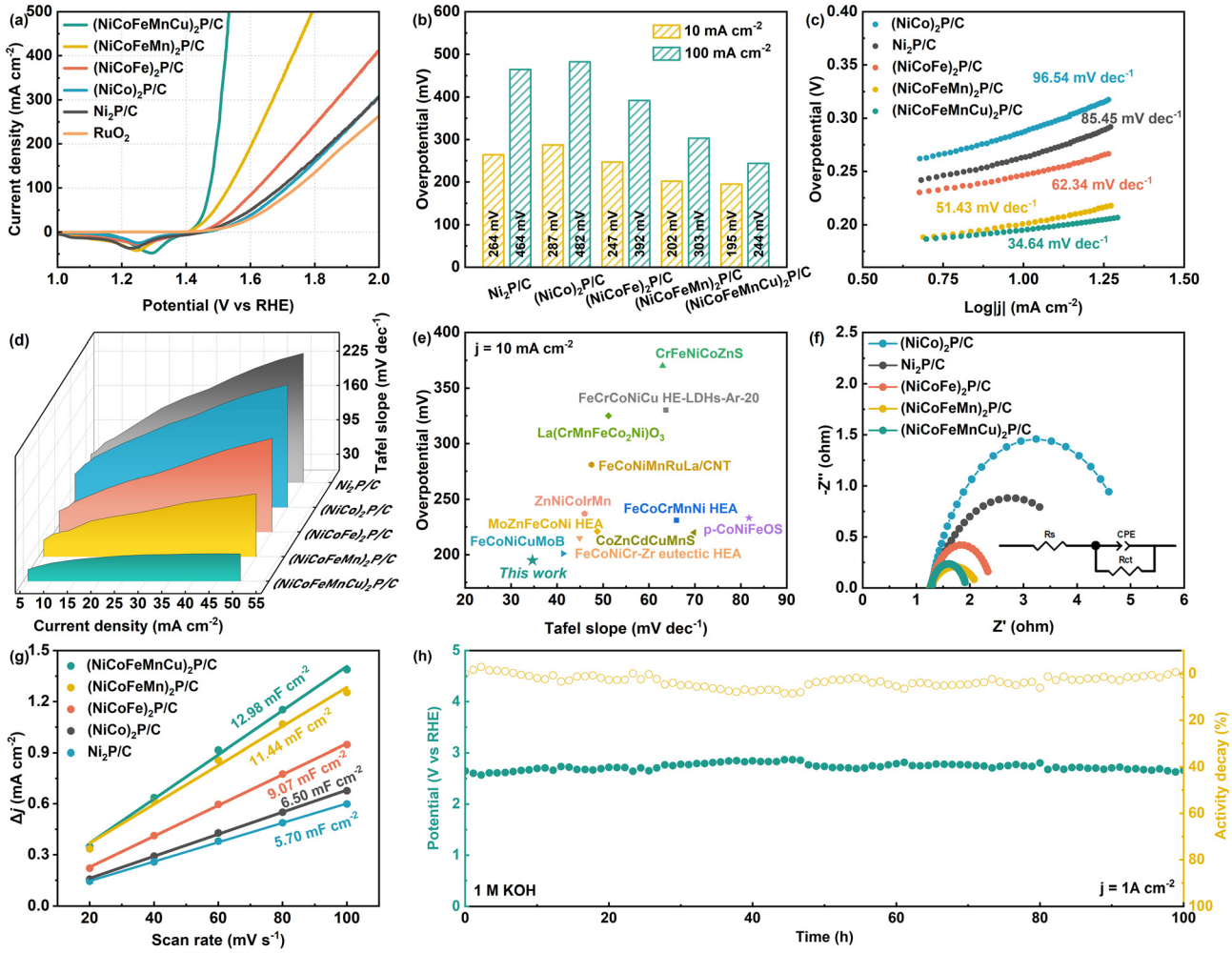

Fig. 4 Electrochemical performance investigation of $(NiCoFeMnCu)_2P/C$ and its counterparts. (a) Polarization curves for the OER, (b) summarized overpotentials at 10 and 100 mA cm^{-2}, (c) corresponding Tafel plots, and (d) Tafel slopes *vs.* average current density of different electrodes. (e) Performance comparison of $(NiCoFeMnCu)_2P/C$ with recently reported high-entropy catalysts in 1 M KOH. (f) Nyquist plots, (g) double-layer capacitance plots and (h) CP curve at 1 A cm^{-2} in 1 M KOH without *iR* correction and corresponding activity decay ratios.

gram (Fig. 4b). Moreover, a low overpotential of 244 mV is achieved even when the current density is increased to 100 mA cm^{-2}, while the corresponding overpotentials of these control samples already exceed 300 mV, indicating the excellent OER activity of the high-entropy electrocatalyst. Tafel slopes as an indicator of OER kinetics were further explored, extracted and fitted from the polarization curves (Fig. 4c). From the unary to quaternary metal phosphide electrocatalyst-based electrodes, the Tafel slopes are 85.45, 96.54, 62.34 and 51.43 mV dec^{-1}. In comparison, the Tafel slope of $(NiCoFeMnCu)_2P$/C/NF is dramatically reduced to 34.64 mV dec^{-1}, demonstrating its faster reaction kinetics than its counterparts. Besides, the Tafel slopes at different average current densities were also determined (Fig. 4d). It can be seen that all Tafel slopes generally increase with the increase of current density, and that of high-entropy $(NiCoFeMnCu)_2P$/C/NF still remains the lowest. Here, one point that needs to be clarified is that although at first the Tafel slope of $(NiCo)_2P$/C/NF is higher than that of the Ni_2P/NF electrode, this situation starts reversing as the current density increases, indicating the important role of Co in promoting the OER kinetics. With such a low overpotential and a very small Tafel slope, the OER activity of the as-prepared $(NiCoFeMnCu)_2P$/C/NF electrode is not only greater than those of the control samples synthesized in this work, but also better than those of most of the reported high-entropy electrocatalysts, as shown in Fig. 4e and Table S2. EIS curves were further collected to reflect the resistance of charge transfer between the electrode surface and the reactants in the electrolyte for evaluating the electrode surface reactivity and transfer characteristics (Fig. 4f). The determined R_{ct} value of $(NiCoFeMnCu)_2P$/C/NF is only 0.67 Ω, lower than those of $(NiCoFeMn)_2P$/C/NF (0.93 Ω), $(NiCoFe)_2P$/C/NF (1.16 Ω), $(NiCo)_2P$/C/NF (3.92 Ω) and Ni_2P/C/NF (3.05 Ω), indicating that the electrons are able to move more quickly across the high-entropy electrocatalyst covered electrode and electrolyte interface, thereby increasing the reaction rate and efficiency of the electrode. In addition, the high-entropy $(NiCoFeMnCu)_2P$/C/NF exhibits the highest C_{dl} value (12.98 mF cm^{-2}), which means that it should also possess a larger ECSA and can provide more active sites for the OER (Fig. 4g and S12). The ECSA was calculated based on the formula in the Experimental section to obtain the ECSA-normalized polarization curves, which are further employed to compare the intrinsic activities of different electrocatalysts (Fig. S13). It can be found that the intrinsic activity of high-entropy $(NiCoFeMnCu)_2P$/C is still superior to those of its counterparts, which manifests that the construction of a high-entropy system is conducive to improving the intrinsic activity of the electrocatalyst. In addition to catalytic activity, stability, especially at high current density, is also a very important indicator for the evaluation of electrocatalyst performance because it is related to industrial practicability. Fig. 4h demonstrates the chrono-potentiometric (CP) curve at an industrial-level current density of 1 A cm^{-2}. One can see that no obvious potential fluctuation occurs even after 100 h of continuous OER operation. The corresponding activity decay ratio was also calculated per 100 min in order to more intuitively assess the stability. As a result, the ratio is always less than 10%, indicating excellent long-term stability at high current density.

Based on the above electrochemical results, a preliminary inference can be further made regarding the specific roles of individual elements. Starting with Ni, it can be observed that pure Ni_2P already exhibits relatively good activity, indicating that Ni phosphate itself possesses excellent OER catalytic activity. The introduction of Co led to a slight decrease in performance, while as the current density increased, the activity of $(NiCo)_2P$ gradually approached that of Ni_2P, and its Tafel slope became lower. This demonstrates that the introduction of Co still modulated the electronic structure and accelerated the reaction kinetics at high current densities. In contrast, the incorporation of Fe significantly enhanced the catalytic activity, validating its role as an electronic structure modulator for NiCo-based catalysts. Its incorporation can optimize the adsorption energy of oxygen intermediates, thereby enhancing OER kinetics. Compared with $(NiCoFe)_2P$, the performance of $(NiCoFeMn)_2P$ improved obviously, manifesting the critical role of Mn in electron modulation and the improved electrical conductivity associated with Mn^{4+}. After the introduction of Cu, a minor reduction in the overpotential at 10 mA cm^{-2} and a significant decrease in the Tafel slope can be observed. This is primarily because the introduction of highly conductive Cu effectively facilitated electron transport within the catalyst layer and to the active sites, which is directly evidenced by the decrease in R_{ct} in EIS results. The improved electron supply kinetics alleviated the limitation imposed by electron transfer in the RDS, thereby leading to a markedly lower Tafel slope.

Meanwhile, the HER performance of the $(NiCoFeMnCu)_2P$/C/NF electrode was also investigated. It is found that the needed overpotential is only 88 mV at 10 mA cm^{-2}, which is significantly lower than those of its counterparts (Fig. S14a), indicating that this electrocatalyst can also be used for the HER. It can be observed that compared to its OER activity, the catalytic performance for the HER is not as remarkable. The probable reason may be that the same sites for the OER may be less optimally tuned for hydrogen intermediate (H*) binding energetics required for ideal HER activity. In addition, the Tafel slope derived from the corresponding polarization curve of high-entropy $(NiCoFeMnCu)_2P$ is 115.77 mV dec^{-1}, which is very close to 120 mV dec^{-1} (Fig. S14b). Hence, it can be deduced that the Volmer step acts as the RDS during the HER in this work.[59] Thus, the binding between the as-synthesized high-entropy catalyst and H may be too weak, resulting in less satisfactory HER activity. Nonetheless, the HER performance remains not so inferior compared to those of reported high-entropy catalysts (Table S2). Regarding future improvements in HER activity, it can be considered from the perspective of further optimizing the composition ratio to further fine-tune the adsorption and desorption behavior of HER intermediates, thereby enhancing hydrogen evolution performance.

Considering the outstanding OER and HER catalytic performance of the high-entropy $(NiCoFeMnCu)_2P$/C in alkaline freshwater electrolyte, its activity was further evaluated in sea-

water-based electrolyte. It can be found that the LSV curves show almost negligible differences in alkaline simulated seawater (1 M KOH + 0.5 M NaCl) and the overpotentials still remain as low as 213 and 88 mV at 10 mA cm^{-2} for the OER and HER, respectively, compared with those in 1 M KOH, indicating that the OER and HER activities of this electrocatalyst are not interfered with by the chloride ions (Fig. 5a and b). Moreover, the achieved current density of $(NiCoFeMnCu)_2P/C/NF$ in alkaline simulated seawater is even higher than that in alkaline freshwater as the applied potential increases, which could result from the stronger conductivity of the alkaline simulated seawater electrolyte originating from the higher ion concentrations. In contrast, when the electrolyte is changed to alkaline natural seawater, a more obvious activity decrease can be observed in the OER and HER, which could be due to the hydroxide precipitation covering the electrocatalyst surface that blocked the active sites. Nonetheless, the overpotentials are still only 223 and 100 mV to achieve 10 mA cm^{-2} in the OER and HER, respectively, lower than those of reported high-entropy materials in alkaline seawater electrolyte (Table S3). As mentioned in the background introduction, the existing chloride ions could induce the anodic competitive CER and electrode corrosion, which are the two main obstacles for seawater splitting. Subsequently, the corrosion resistance and the selectivity were further investigated. The Tafel corrosion curves were first recorded to determine the corrosion potential and current density for assessing the corrosion resistances of the as-prepared electrodes, and the corresponding curves and values are demonstrated in Fig. S15 and Fig. 5d. The smallest corrosion current density and higher corrosion potential value together manifest that the high-entropy $(NiCoFeMnCu)_2P/C/NF$ has higher corrosion resistance. The stable CP curves remain stable for at least 100 h under ampere-level current density in both alkaline simulated and natural seawater electrolytes (Fig. 5e and f), further demonstrating its exceptional stability and corrosion resistance. Herein, its excellent stability and corrosion resistance can be attributed to the intrinsic structural stability provided by the high-entropy sluggish diffusion effect. The sluggish diffusion effect, recognized as one of the four core effects in HEMs, refers to the significantly

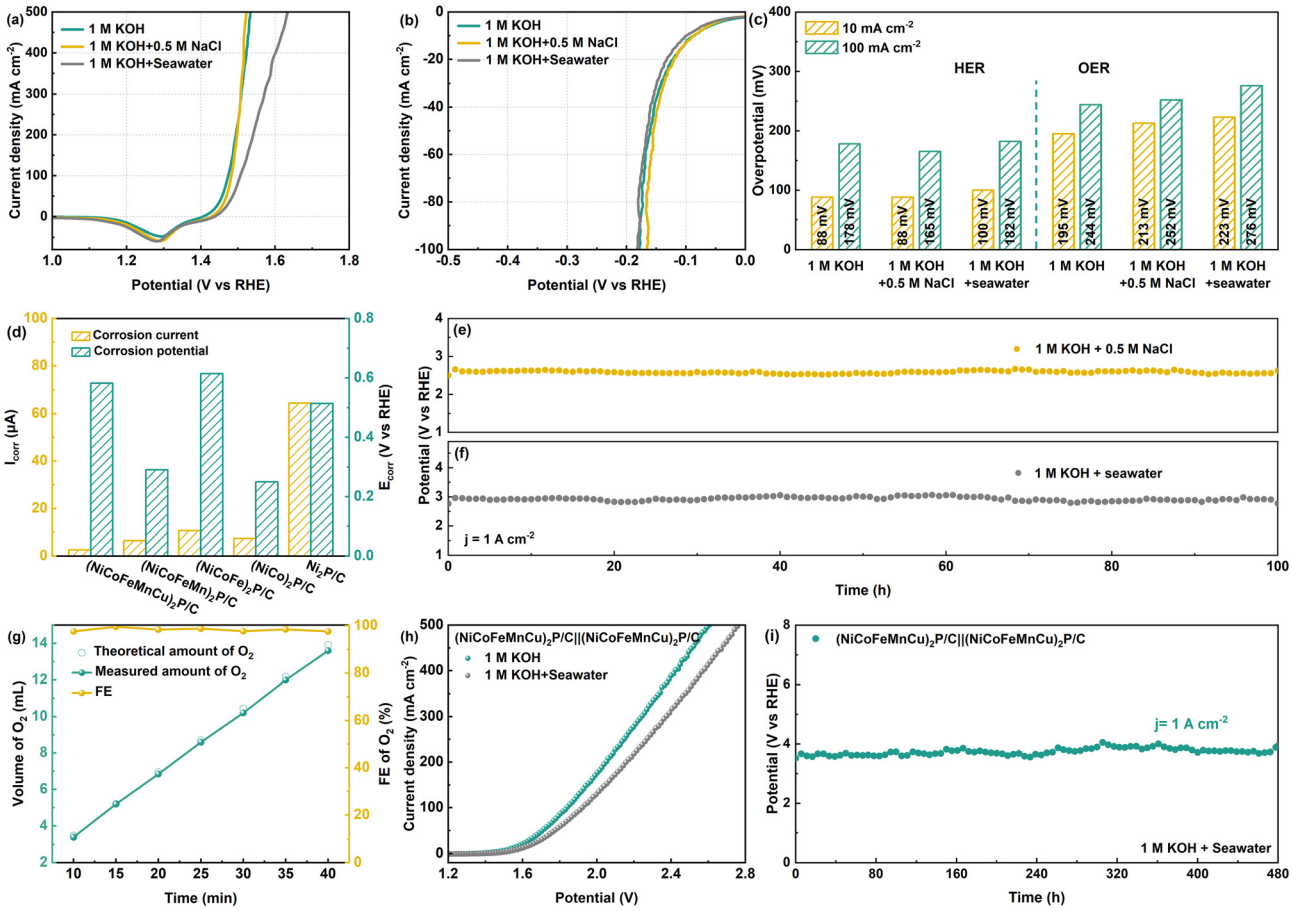

Fig. 5 Electrochemical performance in different electrolytes of $(NiCoFeMnCu)_2P/C$. Polarization curves for (a) the OER and (b) the HER of the $(NiCoFeMnCu)_2P/C/NF$ electrode in different electrolytes and (c) summarized overpotentials at 10 and 100 mA cm^{-2}. (d) Corrosion currents and potentials of different catalysts. CP curves in (e) 1 M KOH + 0.5 M NaCl and (f) 1 M KOH + seawater at 1 A cm^{-2}. (g) FEs in 1 M KOH + seawater. (h) Polarization curves of the $(NiCoFeMnCu)_2P/C/NF||(NiCoFeMnCu)_2P/C/NF$ cell in 1 M KOH and 1 M KOH + seawater. (i) CP curve of the $(NiCoFeMnCu)_2P/C/NF||(NiCoFeMnCu)_2P/C/NF$ cell in 1 M KOH + seawater at 1 A cm^{-2}.

reduced atomic diffusion rates within their structures due to multiple constraining factors.[13,60] Owing to the presence of numerous constituent elements, atomic movement in these materials is hindered by lattice defects, interactions with surrounding atoms, and inter-element effects, which collectively increase the energy barrier for atom diffusion and surface degradation.[61] As a result, HEMs often exhibit superior structural stability and corrosion resistance. This makes it difficult for chloride ions to penetrate or destroy the material's surface structure, thereby improving its durability in seawater electrolytes.[62,63] In addition, *N*,*N*-diethyl-1,4-phenylenediamine (DPD) was employed as an indicator to verify the generation of hypochlorite species during the electrolysis process through UV-Vis measurements (the detailed testing process can be found in the SI). As displayed in Fig. S16, the UV-vis spectrum of the electrolyte after long-term stability testing only demonstrates weak adsorption peaks at ~551 nm with an intensity even lower than 0.1 ppm of ClO^-, which jointly indicates negligible hypochlorite species formation, confirming the high OER selectivity of high-entropy $(NiCoFeMnCu)_2P/C$. The FE was also calculated based on the equation as shown in the Experimental section, where the actual produced amount of oxygen was obtained through the drainage method. Based on the determined results, the corresponding FE at each point was calculated (Fig. 5g), and the average FE is around 98.30%, indicating high OER selectivity of the high-entropy phosphate electrocatalyst. In view of the impressive bifunctional catalytic activity, $(NiCoFeMnCu)_2P/C$ was also applied for overall water/seawater splitting, achieving a current density of 10 mA cm^{-2} at 1.53 and 1.58 V, respectively (Fig. 5h). Specifically, the two-electrode cell exhibits excellent long-term stability, sustaining continuous overall seawater electrolysis for up to 480 h even at an industrial-level current density of 1 A cm^{-2} (Fig. 5i). Thus, this electrocatalyst should be a promising candidate for practical overall seawater splitting.

Structural evolution investigation and mechanism elucidation

Post-stability structural characterization was also conducted to investigate the structural evolution and possible reaction mechanism. Morphological characterization first reveals that the catalyst retains its intact nanosheet morphology after the stability test (Fig. S17). According to the results of TEM observation (Fig. 6a), it can be seen that the catalyst retains its high-entropy nanoparticles/carbon composite morphology. In addition, the lattice fringes observed by HRTEM are measured with the lattice spacings of 0.204, 0.205 and 0.236 nm that correspond to the (111), (111) and (201) crystal planes, respectively (Fig. 6b), which are consistent with the initial as-synthesized electrocatalyst. The existence of all constituent elements is also proved by EDX elemental maps of the spent electrocatalyst (Fig. S18). Moreover, the high-resolution XPS spectra of all constituent elements were also explored to elucidate the surface chemical state transformations. From the comparison of Ni 2p XPS spectra before and after the long-term OER (Fig. 6c), one can see that the characteristic peaks of Ni^0 completely disappear with only XPS peaks of Ni^{2+} and Ni^{3+} remaining, indicating that Ni^0 has been fully oxidized during long-term usage. The high-resolution XPS spectrum of Co 2p can still be divided into those of Co^{3+} and Co^{2+} (Fig. 6d) while the proportion of Co^{3+} increases from 51.01 to 64.18%, which signifies partial oxidation. As for the Fe 2p XPS spectrum (Fig. 6e), although Fe still persists in the forms of Fe^{2+} and Fe^{3+}, it is obvious that Fe^{3+} becomes dominant in the spent electrocatalyst (*ca.* 50.84%) when compared with that in the pristine high-entropy electrocatalyst (*ca.* 26.40%). The Mn 2p XPS spectrum after the stability test demonstrates main peaks corresponding to Mn^{2+}, Mn^{3+} and Mn^{4+} species (Fig. 6f), but a higher ratio of Mn^{4+} is observed in contrast to the pristine one. In addition, the proportion of Mn^{2+} is observed to increase; therefore, it can be deduced that Mn probably only plays a role in electron modulation. Based on the Cu 2p XPS spectrum (Fig. 6g), the proportions of Cu^+ and Cu^{2+} exhibit no significant changes, meaning that the surface Cu is barely affected. The corresponding ratios of different elements with various valence states are also summarized in Table S4, collectively indicating that the surface oxidation selectively occurs on certain metal sites (*i.e.*, Fe, Co and Ni). Overall, the increases in the valence states of the metal elements on the high-entropy phosphide surface after the long-term testing indicate electrode surface oxidation. This speculation is further corroborated by the disappearance of the M–P peak in the P 2p XPS spectrum (Fig. 6h). Additionally, a characteristic XPS peak of the M–OH group newly emerges in the O 1s spectrum (Fig. 6i), further jointly verifying the formation of metal (oxy)hydroxide (MOOH) on the catalyst surface. The reconstructed layer is not only widely recognized as the active site but also can serve as a protective barrier that repels Cl^- and prevents its approach to the reactive centers,[64,65] thereby providing further explanation for the catalyst's exceptional selectivity and stability.

Subsequently, further investigation and discussion of the OER mechanism were conducted. Initially, the pH dependence was investigated by recording polarization curves in electrolytes with different pH levels. Based on these results, the proton reaction order ($\rho^{RHE} = \partial\log(j)/\partial pH$) can be calculated. The magnitude of ρ^{RHE} provides initial insights into the reaction mechanism. When the OER involves proton-coupled electron transfer, its kinetics are largely independent of the solution pH, resulting in a low proton reaction order. Conversely, if the OER proceeds through non-synergistic proton electron transfer, its kinetics strongly depend on pH, which would lead to a high ρ^{RHE}.[66] The experimental results showed significant changes in catalytic activity with varying pH, along with a notably high ρ^{RHE} (0.94) close to 1.0 (Fig. S19a and b). This suggests that the OER mechanism most likely follows the lattice oxygen oxidation mechanism (LOM) rather than the conventional adsorbate evolution mechanism (AEM).[67,68] Moreover, unlike the AEM, the LOM generates O_2^{2-} species during the OER. Therefore, detecting O_2^{2-} is crucial for verifying the OER pathway. To further confirm the reaction mechanism, we introduced tetramethylammonium cations (TMA^+), which can strongly interact with O_2^{2-} species and inhibit OER kinetics, thus serving as a probe

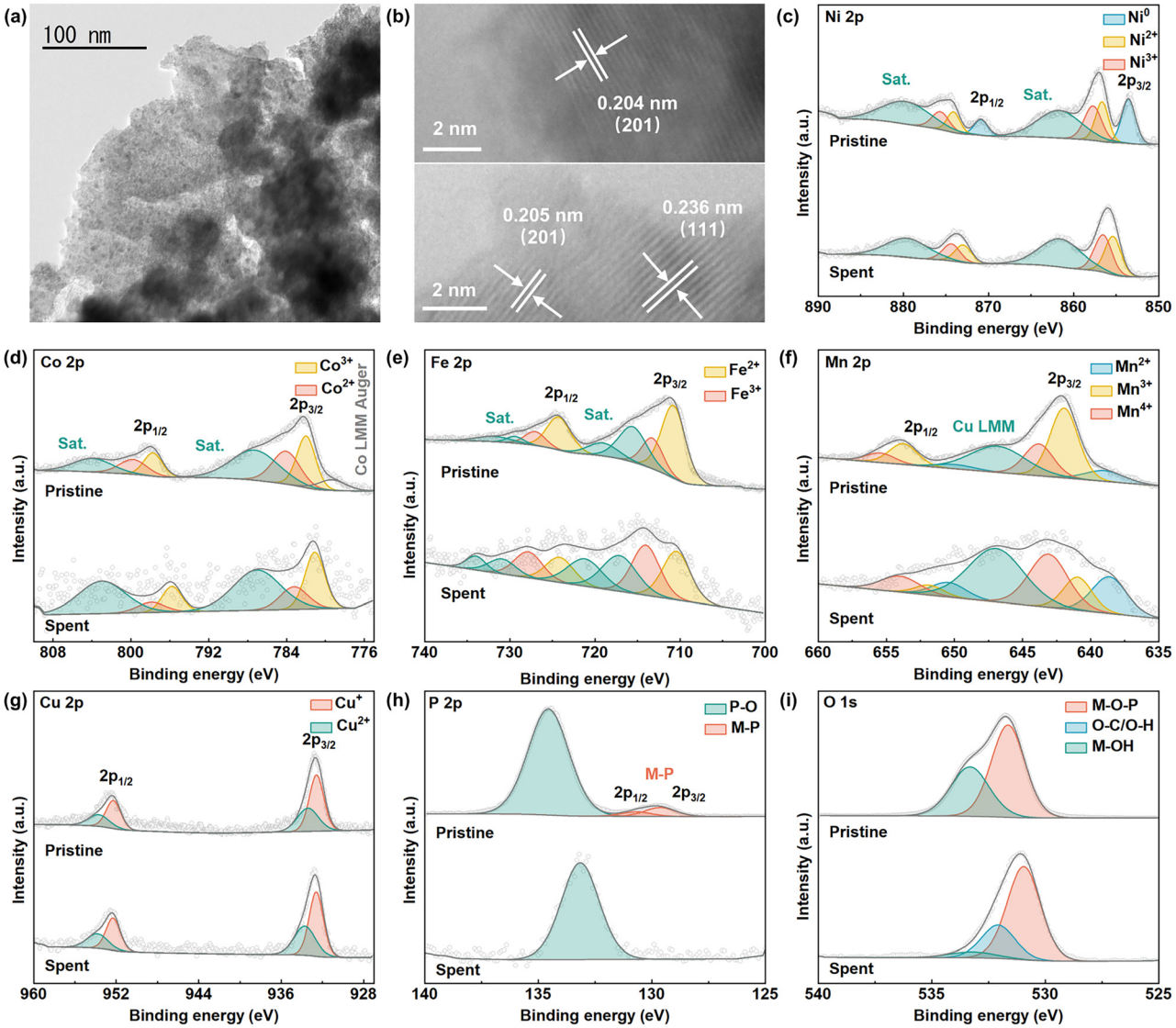

Fig. 6 Post-characterization of spent $(NiCoFeMnCu)_2P$/C. (a) TEM image, (b) HRTEM image, and high-resolution XPS spectra for (c) Ni 2p, (d) Co 2p, (e) Fe 2p, (f) Mn 2p, (g) Cu 2p, (h) P 2p and (i) O 1s.

for such intermediates.[69] As shown in Fig. S19c and d, the OER activity of HEP/C is significantly lower in 1.0 M TMAOH electrolyte than that in 1.0 M KOH electrolyte ($\Delta\eta_{100}$ = 0.08 V and ΔTafel = 17.03 mV dec^{-1}). This indicates a strong interaction between TMA^+ and O_2^{2-}, confirming that HEP/C follows the LOM pathway during the OER.

Conclusions

This work establishes MOF-derived HEP/C as a transformative electrocatalytic platform for sustainable hydrogen production *via* seawater electrolysis. The high-entropy catalyst, integrating five transition metals, achieves exceptional bifunctionality with ultra-low overpotentials of 88/195 mV (HER/OER) in alkaline freshwater and 100/223 mV in seawater at 10 mA cm^{-2}. Furthermore, the HEP/C based electrode assembled into a two-electrode electrolyzer demonstrates low driven voltages of 1.53 and 1.58 V at 10 mA cm^{-2} for overall freshwater and seawater splitting, respectively. Robust chloride resistance is also evidenced by continuous stable operation for 480 hours without obvious activity decay, and the near absence of hypochlorite species in the electrolyte confirms the high selectivity. The HEP/C catalytic system reconciles critical activity–selectivity–stability trade-offs through the integration of: (i) the intrinsic activity of TMP-integrated high-entropy induced multi-metal synergy; (ii) the generated conductive carbon matrix that enhances charge transfer while inhibiting chloride penetration; and (iii) *in situ* reconstructed MOOH layers that serve as active sites and provide a protective shield for the catalyst against corrosion. Ultimately, the entropy

engineering of HEP/C electrocatalysts paves a practical way toward large-scale hydrogen production economies through seawater electrolysis. This work highlights the great potential of MOF-derived HEPs as promising bifunctional electrocatalysts for efficient seawater splitting.

Author contributions

Changrui Feng: writing – review & editing, validation, resources, methodology, investigation, formal analysis, data curation, and conceptualization. Yifan Zhou: writing – original draft, visualization, validation, methodology, investigation, formal analysis, data curation, and conceptualization. Shuying Li: investigation. Yuxia Jin: investigation. Meng Chen: investigation. Rui Yang: investigation. Wenjia Zhou: investigation. Zhengkun Xie: investigation and writing – review & editing. Xiumin Li: investigation. Xiangyu Chen: investigation. Abuliti Abudula: investigation. Guoqing Guan: writing – review & editing, supervision, project administration, funding acquisition, formal analysis, data curation, and conceptualization.

Conflicts of interest

There are no conflicts to declare.

Data availability

All relevant data supporting this article have been included in the main text and the SI or can be obtained from the corresponding author upon reasonable request.

Supplementary information is available. The morphological and structural information of control samples, electrochemical verification of reaction mechanism, and performance comparison are included there. See DOI: **https://doi.org/10.1039/d5gc03723a**.

Acknowledgements

This work is supported by the Hirosaki University Fund, Japan. The authors acknowledge the Shared Facility Center for Science and Technology (SFCST), Hirosaki University, Japan, for TEM-EDX, XRD and SEM-EDX measurements.

References

1 Y. Ou, L. Liu, X. Peng, L. Zhang, Z. Ou, W. Zhang and Y. Zhang, *Nano Mater. Sci.*, 2024, **6**, 565.
2 Y.-N. Zhou, W.-L. Yu, H.-J. Liu, R.-Y. Fan, G.-Q. Han, B. Dong and Y.-M. Chai, *EcoEnergy*, 2023, **1**, 425.
3 D. Sui, R. Luo, S. Xie, H. Zhang, T. Ma, H. Sun, T.-T. Jia, J. Sun and X. Li, *Chem. Eng. J.*, 2024, **480**, 148007.
4 M. S. A. Sher Shah, G. Y. Jang, K. Zhang and J. H. Park, *EcoEnergy*, 2023, **1**, 344.
5 N. Johnson, M. Liebreich, D. M. Kammen, P. Ekins, R. McKenna and I. Staffell, *Nat. Rev. Clean Technol.*, 2025, **1**, 351.
6 J. T. Ren, L. Chen and Z. Y. Yuan, *Mater. Today*, 2025, **86**, 282.
7 I. W. Ock, J. Yin, S. Wang, X. Zhao, J. M. Baik and J. Chen, *Adv. Energy Mater.*, 2025, **15**, 2400563.
8 X. Fu, X. Zang, J. Gao, H. Li, W. Xiao, Y. Zong, G. Fu, J. Wang, T. Ma, W. Jin, Z. Wu and L. Wang, *Adv. Energy Mater.*, 2025, **15**, 2501054.
9 Y. Wang, J. Li, P. Yang, H. Li, G. Xu, Y. Du, C. Li, W. Jin, T. Ma, Z. Wu and L. Wang, *J. Energy Chem.*, 2025, **102**, 618.
10 H. Jin, J. Xu, H. Liu, H. Shen, H. Yu, M. Jaroniec, Y. Zheng and S.-Z. Qiao, *Sci. Adv.*, 2023, **9**, eadi7755.
11 R. Fan, C. Liu, Z. Li, H. Huang, J. Feng, Z. Li and Z. Zou, *Nat. Sustainability*, 2024, **7**, 158.
12 J. Li, G. Fu, X. Sheng, G. Li, H. Chen, K. Shu, Y. Dong, T. Wang and Y. Deng, *Adv. Powder Mater.*, 2024, **3**, 100227.
13 Y. Ma, Y. Ma, Q. Wang, S. Schweidler, M. Botros, T. Fu, H. Hahn, T. Brezesinski and B. Breitung, *Energy Environ. Sci.*, 2021, **14**, 2883.
14 D. Liu, P. Guo, H. Pan and R. Wu, *Prog. Mater. Sci.*, 2024, **145**, 101300.
15 J. Cai and H. Zhu, *Commun. Mater.*, 2025, **6**, 118.
16 Y. Wan, W. Wei, S. Ding, L. Wu, H. Qin and X. Yuan, *Adv. Funct. Mater.*, 2025, **35**, 2414554.
17 B. Wang, J. Ma, K. Wang, D. Wang, G. Xu, X. Wang, Z. Hu, C.-W. Pao, J.-L. Chen, L. Du, X. Du and G. Cui, *Adv. Energy Mater.*, 2024, **14**, 2401090.
18 C. Feng, Y. Zhou, Z. Xie, Z. Yang, L. Zou, P. Wang, W. Lian, P. Xiaokaiti, Y. Kansha, A. Abudula and G. Guan, *Chem. Eng. J.*, 2024, **495**, 153408.
19 H. Zhou, J. R. Long and O. M. Yaghi, *Chem. Rev.*, 2012, **112**, 673.
20 Y. Zhou, L. Gao, H. Chen, H. Wang, J. Zhang, X. Li, F. Duo and G. Guan, *J. Mater. Sci. Technol.*, 2024, **168**, 62.
21 Y. Yuan, K. Wang, B. Zhong, D. Yu, F. Ye, J. Liu, J. Dutta and P. Zhang, *Energy Environ. Mater.*, 2024, **7**, e12747.
22 C. Huang, Q. Zhou, L. Yu, D. Duan, T. Cao, S. Qiu, Z. Wang, J. Guo, Y. Xie, L. Li and Y. Yu, *Adv. Energy Mater.*, 2023, **13**, 2301475.
23 N. Khodayar, A. Noori, M. S. Rahmanifar, M. Moloudi, N. Hassani, M. Neek-Amal, M. F. El-Kady, N. B. Mohamed, X. Xia, Y. Zhang, R. B. Kaner and M. F. Mousavi, *Energy Environ. Sci.*, 2024, **17**, 5200.
24 R. Deng, M. Guo, C. Wang and Q. Zhang, *Nano Mater. Sci.*, 2024, **6**, 139.
25 Z. Wu, Q. Li, G. Xu, W. Jin, W. Xiao, Z. Li, T. Ma, S. Feng and L. Wang, *Adv. Mater.*, 2024, **36**, 2311018.
26 A. F. Payam, S. Khalil and S. Chakrabarti, *Small*, 2024, **20**, 2310348.
27 X. F. Lu, Y. Fang, D. Luan and X. W. D. Lou, *Nano Lett.*, 2021, **21**, 1555.
28 Z. Pu, T. Liu, I. S. Amiinu, R. Cheng, P. Wang, C. Zhang, P. Ji, W. Hu, J. Liu and S. Mu, *Adv. Funct. Mater.*, 2020, **30**, 2004009.

29 Q. Wang, K. Dastafkan and C. Zhao, *Curr. Opin. Electrochem.*, 2018, **10**, 16.
30 X. Li, W. Xing, T. Hu, K. Luo, J. Wang and W. Tang, *Coord. Chem. Rev.*, 2022, **473**, 214811.
31 A. R. J. Kucernak and V. N. Naranammalpuram Sundaram, *J. Mater. Chem. A*, 2014, **2**, 17435.
32 X. Li, S. Guo, W. Li, X. Ren, J. Su, Q. Song, A. J. Sobrido and B. Wei, *Nano Energy*, 2019, **57**, 388.
33 B. Cao, G. M. Veith, J. C. Neuefeind, R. R. Adzic and P. G. Khalifah, *J. Am. Chem. Soc.*, 2013, **135**, 19186.
34 P. M. Bodhankar, P. B. Sarawade, P. Kumar, A. Vinu, A. P. Kulkarni, C. D. Lokhande and D. S. Dhawale, *Small*, 2022, **18**, 2107572.
35 S. Guo, Q. Lu, X. Zhou, Y. Wang, M. Li and B. Liu, *Energy Fuels*, 2025, **39**, 7915.
36 S. Yang, X. Liu, S. Li, W. Yuan, L. Yang, T. Wang, H. Zheng, R. Cao and W. Zhang, *Chem. Soc. Rev.*, 2024, **53**, 5593.
37 M. S. Burke, M. G. Kast, L. Trotochaud, A. M. Smith and S. W. Boettcher, *J. Am. Chem. Soc.*, 2015, **137**, 3638.
38 V. Chakrapani, C. Wang, Q. Wang and N. Smieszek, *Surf. Interface Anal.*, 2022, **54**, 1192.
39 Y. Gan, M. Cui, X. Dai, Y. Ye, F. Nie, Z. Ren, X. Yin, B. Wu, Y. Cao, R. Cai and X. Zhang, *Nano Res.*, 2022, **15**, 3940.
40 S. Wang, X. Shen, H. Jin, Y. Su, N. Li, J. Li, Z. Xiong, C. Feng and Y. Zhao, *J. Alloys Compd.*, 2025, **1038**, 182933.
41 K. Kannimuthu, K. Sangeetha, S. Sam Sankar, A. Karmakar, R. Madhu and S. Kundu, *Inorg. Chem. Front.*, 2021, **8**, 234.
42 S. Ran, J. Qi, X. Dong, H. Huang, M. Qi, W. Dong, P. Zhao, Z. Zhao and J. Yang, *Chem. Eng. J.*, 2023, **463**, 142174.
43 H. Huang, M. Cheng, J. Yin, J. Zhang, L. Kong and X.-H. Bu, *Electrochim. Acta*, 2022, **426**, 140794.
44 S. Liu, W. Xu, K. Feng, X. Shi and C. Wang, *J. Energy Storage*, 2024, **96**, 112684.
45 F. Sun, G. Wang, Y. Ding, C. Wang, B. Yuan and Y. Lin, *Adv. Energy Mater.*, 2018, **8**, 1800584.
46 J. Zhou, Z. Han, X. Wang, H. Gai, Z. Chen, T. Guo, X. Hou, L. Xu, X. Hu, M. Huang, S. V. Levchenko and H. Jiang, *Adv. Funct. Mater.*, 2021, **31**, 2102066.
47 M. A. Pimenta, G. Dresselhaus, M. S. Dresselhaus, L. G. Cançado, A. Jorio and R. Saito, *Phys. Chem. Chem. Phys.*, 2007, **9**, 1276.
48 T. Wang, X. Guo, J. Zhang, W. Xiao, P. Xi, S. Peng and D. Gao, *J. Mater. Chem. A*, 2019, **7**, 4971.
49 N. Yang, C. Tang, K. Wang, G. Du, A. M. Asiri and X. Sun, *Nano Res.*, 2016, **9**, 3346.
50 S. Wang, W. Huo, F. Fang, Z. Xie, J. K. Shang and J. Jiang, *Chem. Eng. J.*, 2022, **429**, 132410.
51 A. A. Ahmad, T. G. Ulusoy Ghobadi, E. Ozbay and F. Karadas, *Chem. Commun.*, 2022, **58**, 9341.
52 X. Li, Z. Xie, S. Roy, L. Gao, J. Liu, B. Zhao, R. Wei, B. Tang, H. Wang, P. Ajayan and K. Tang, *Adv. Mater.*, 2025, **37**, 2410295.
53 T. Li, Y. Hu, K. Liu, J. Yin, Y. Li, G. Fu, Y. Zhang and Y. Tang, *Chem. Eng. J.*, 2022, **427**, 131992.
54 Z. Li, X. Wu, X. Jiang, B. Shen, Z. Teng, D. Sun, G. Fu and Y. Tang, *Adv. Powder Mater.*, 2022, **1**, 100020.
55 Z. Lu, L. Qian, Y. Tian, Y. Li, X. Sun and X. Duan, *Chem. Commun.*, 2016, **52**, 908.
56 Y. Zhou, C. Feng, M. Chen, Z. Yang, L. Gao, S. Li, J. Wang, X. Li, Y. Kansha, A. Abudula and G. Guan, *Int. J. Hydrogen Energy*, 2024, **87**, 771.
57 K. Zhou, W. Zhou, L. Yang, J. Lu, S. Cheng, W. Mai, Z. Tang, L. Li and S. Chen, *Adv. Funct. Mater.*, 2015, **25**, 7530.
58 A. V. Shchukarev and D. V. Korolkov, *Cent. Eur. J. Chem.*, 2004, **2**, 347.
59 J. Zhu, L. Hu, P. Zhao, L. Y. S. Lee and K.-Y. Wong, *Chem. Rev.*, 2020, **120**, 851.
60 W. Wang, Q. Zhang, L. Yang, G. Liang, X. Xiong, Y. Cheng, L. Wu, C. Lin and R. Che, *Adv. Sci.*, 2025, **12**, 2411291.
61 W.-L. Hsu, C.-W. Tsai, A.-C. Yeh and J.-W. Yeh, *Nat. Rev. Chem.*, 2024, **8**, 471.
62 I. C. Chiu, C.-Y. Chiang, H.-Y. Chang, C.-T. Li, H.-Y. Chi, H.-C. Huang, P. Chang, Y.-T. Wang, R. Lee, I. Y. Tsao, C.-L. Chiang, B. K. Chang, Y.-G. Lin and W. H. Hung, *Sustainable Mater. Technol.*, 2025, **45**, e01515.
63 Y. Xie, S. Xu, A. C. Meng, B. Zheng, Z. Chen, J. M. Tour and J. Lin, *Energy Environ. Sci.*, 2024, **17**, 8670.
64 S. Li, K. Wang, C. Liang, H. Wu, J. Li, Y. Wang, L. Lei, M. Zhu, L. Zhuang and Z. Xu, *Chem Catal.*, 2023, **3**, 100789.
65 C. Wang, M. Zhu, Z. Cao, P. Zhu, Y. Cao, X. Xu, C. Xu and Z. Yin, *Appl. Catal., B*, 2021, **291**, 120071.
66 X. Chen, Q. Wang, Y. Cheng, H. Xing, J. Li, X. Zhu, L. Ma, Y. Li and D. Liu, *Adv. Funct. Mater.*, 2022, **32**, 2112674.
67 C. Lin, J.-L. Li, X. Li, S. Yang, W. Luo, Y. Zhang, S.-H. Kim, D.-H. Kim, S. S. Shinde, Y.-F. Li, Z.-P. Liu, Z. Jiang and J.-H. Lee, *Nat. Catal.*, 2021, **4**, 1012.
68 F. Wang, P. Zou, Y. Zhang, W. Pan, Y. Li, L. Liang, C. Chen, H. Liu and S. Zheng, *Nat. Commun.*, 2023, **14**, 6019.
69 Z.-F. Huang, S. Xi, J. Song, S. Dou, X. Li, Y. Du, C. Diao, Z. J. Xu and X. Wang, *Nat. Commun.*, 2021, **12**, 3992.